

Electric field-induced interfacial instability in a ferroelectric nematic liquid crystal

Marcell Tibor Máthé^{1,2}, Bendegúz Farkas^{1,2}, László Péter¹, Ágnes Buka¹, Antal Jáklí^{1,3,4,*},
Péter Salamon^{1,*}

¹Institute for Solid State Physics and Optics, Wigner Research Centre for Physics, P.O. Box 49, Budapest H-1525, Hungary

²Eötvös Loránd University, P.O. Box 32, H-1518 Budapest, Hungary

³Materials Sciences Graduate Program and Advanced Materials and Liquid Crystal Institute, Kent State University, Kent, Ohio 44242, USA

⁴Department of Physics, Kent State University, Kent, Ohio 44242, USA

*: Author for correspondence: salamon.peter@wigner.hu

Abstract

Studies of sessile droplets and fluid bridges of a ferroelectric nematic liquid crystal in externally applied electric fields are presented. It is found that above a threshold a fingering instability occurs, resembling to Rayleigh-type instability observed in charged droplets in electric fields or circular drop-type instabilities observed in ferromagnetic liquids in magnetic field. The frequency dependence of the threshold voltage was determined in various geometries. The nematic director and ferroelectric polarization direction was found to point along the tip of the fingers that appear to repel each other, indicating that the ferroelectric polarization is essentially parallel to the director. The results are interpreted in analogy to the Rayleigh and circular drop-type instabilities.

I. Introduction

Conventional nematic (N) liquid crystals (LC) are usually formed by elongated organic molecules. In a continuum description, the local symmetry axis of nematics is defined by the average molecular orientation, which is called the director (\hat{n})¹. $N - LC$ s have already achieved significant impact in our modern life as being the bases of the currently dominant display technology. In flat display technology, where dielectric nematic liquid crystals are utilized, the high frequency (AC) electric field-induced director reorientation results in the electro-optical effect allowing to control the brightness of each pixel in a display². An important property of

the nematic phase is the “head–tail” symmetry, i.e., $\hat{n} = -\hat{n}$. This head–tail symmetry is broken in the ferroelectric nematic (N_F) phase due to the spontaneous polarization \vec{P}_s , where the director becomes a vector \vec{n} that is assumed to be parallel to \vec{P}_s ^{3,4}. The existence of a ferroelectric liquid nematic phase was proposed already in 1916^{5,6} by Max Born to explain the isotropic-nematic phase transition. Although it turned out that ferroelectricity is not needed for the existence of a nematic phase, scientists were looking for the N_F phase over a century, but there were no unambiguous experimental indications of it until the syntheses of the highly polar rod-shaped compounds referred to as DIO and RM734 by Nishikawa et al.⁷ and Mandle et al.^{8,9}, respectively in 2017. The N_F phase of RM734 was first suggested to have splayed polar order^{10–12}, but more recently, it was shown that it has a uniform ferroelectric nematic phase³. RM734 and DIO have large molecular dipole moments of about 10 Debye, and a spontaneous polarization up to $|\vec{P}_s| \sim 5 \mu\text{C}/\text{cm}^2$. The apparent dielectric permittivity and its anisotropy were reported to be orders of magnitude higher than those of classical nematics, reaching $\varepsilon \sim 10^4$ or higher^{7,11,13–18} implying an extremely large sensitivity of the N_F materials to electric fields. Such a large dielectric constant suggests a giant dielectrowetting at unprecedentedly low voltages, since its threshold scales with the square root of the fluid’s permittivity^{19–21}. Furthermore, in analogy to the spectacular Rosensweig instability²² of ferromagnetic fluids in magnetic field, one can expect to see electric field induced spike patterns in ferroelectric fluids with free surface. A hint of such instability was demonstrated by Barboza et al.²³ who showed that sessile droplets of RM734 become unstable and disintegrate through the emission of fluid jets when they are deposited on a lithium niobate (LN) ferroelectric crystal substrate. This phenomenon was explained in analogy to the Rayleigh instability²⁴ of charged fluid droplets. Cmok et al. presented the behavior of sessile ferroelectric nematic droplets on LN surfaces exposed to light^{25,26}.

In this paper, we show that Rosensweig-type instabilities observed in ferromagnetic liquids in magnetic field and Rayleigh-type instability observed in charged droplets, can be also induced in ferroelectric nematic sessile droplets and bridges by externally applied AC electric fields. In addition to quantitative measurements in various geometries, we will also theoretically analyze the results.

II. Experimental results

We have studied the effect of AC electric fields in three different geometries: electric voltage applied normal to the base plane of a sessile droplet (G1), and of a fluid bridge (G2),

and electric field applied along the base plane of a sessile droplet (G3). Unless it is indicated differently, all measurements were carried out about 5 °C below the $N - N_F$ phase transition.

The experimental geometry of G1 and the responses to $f = 10$ kHz 210 V, 220 V and 300 V rms AC electric voltages applied between the base plate and another ITO coated plate placed at $L = 150$ μm distance, are shown in Figure 1. At and below 210 V the droplet is stable, while above it, the ejection of several thin jets can be observed. Some of them are decorated with additional secondary jets like that observed by Barboza et al²³. The structure is stationary at a given voltage (see Supplementary Video 1).

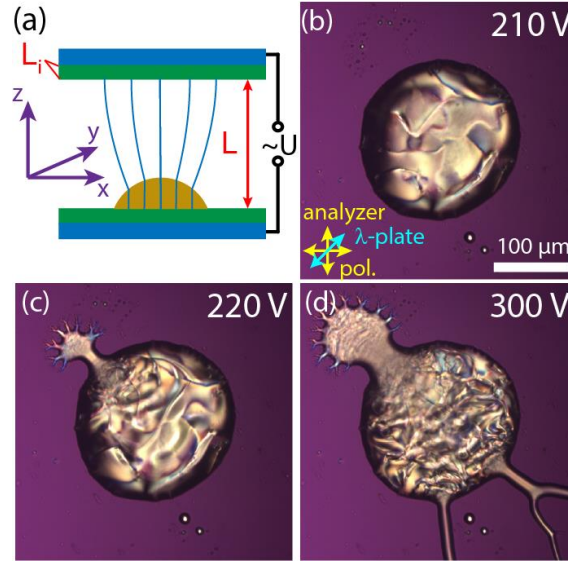


Figure 1: A ferroelectric nematic sessile droplet in electric fields along the normal direction of the base plate. (a) Illustration of the G1 geometry with approximate electric field (green lines) and coordinate system. (b-d) Polarizing optical microscopy images of a ferroelectric nematic sessile droplet between crossed polarizers (yellow arrows) and a full-wave plate ($\lambda=546$ nm - blue arrow) at 210 V, 220 V and 300 V, respectively.

The G2 geometry and a typical response to electric fields of an N_F bridge with $L = 74$ μm thickness is shown in Figure 2. In the isotropic and nematic phase, the circumferences of the contact lines on the bottom and top bounding plates start to grow above a certain threshold voltage, while keeping their original round shape (Figure 2b). In contrast to this behavior, in the ferroelectric nematic phase (Figure 2c) the contact line becomes unstable and a fractal-like spreading of the fluid is observed (see Supplementary Video 2 in case of another droplet). Inside the droplet at high voltage, electro-hydrodynamic convection takes place that is stronger near the perimeter of the droplets. To precisely analyze the voltage dependence of the electric field induced interfacial instability, we applied a geometrical transformation, mapping a band around the contact line to a rectangle (Figure 2d), which we will further discuss below. In Figure 2e, we show the side view of a liquid bridge exposed to high voltage, clearly demonstrating that the instability forms in the vicinity of the glass plates.

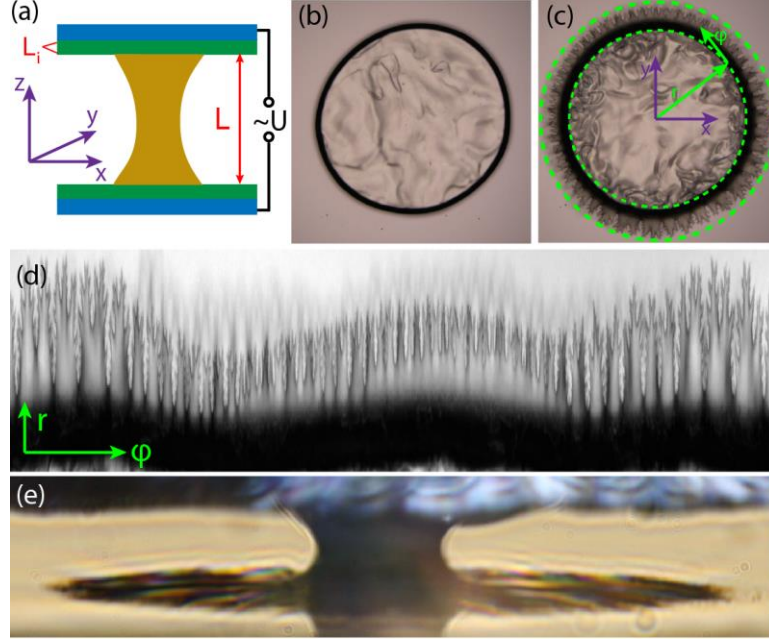


Figure 2: A ferroelectric nematic fluid bridge in electric field along the normal direction of the base plate. (a) Illustration of the G2 geometry with approximate electric field and coordinate system. (b) Top view of a fluid bridge at zero voltage ($558 \mu\text{m}$ diameter, $74 \mu\text{m}$ thickness) and (c) at $f=800 \text{ Hz}$, 52 V AC voltage. (d) Transformed view of the perimeter of the bridge exhibiting the instability. Darker (lighter) pattern shows the instability at the top (bottom) glass. (e) Side view of the bridge clearly indicates that the instability forms in the vicinity of the electrodes.

Using the transformed image of the perimeter of the droplet, we calculated a specific type of roughness of the contact line denoted by Ro_{cl} and defined in detail in the Methods section. Ro_{cl} gives a quantitative indicator for the emergence of the interfacial instability, while being insensitive to the gradual growth of the circumference due to electrowetting.

Figure 3 shows the schematics of the in-plane electrode geometries (G3) together with microphotographs of ferroelectric nematic droplets. Figure 3a illustrates the interdigitated electrodes with the coordinate system, while Figure 3b and c show the side view ($x - z$ plane) of the electrodes with the fringing field, and the sessile droplet, respectively. The top-view ($x - y$ plane) of the reflection microscopy images of a droplet at zero voltage and with $f = 10 \text{ kHz}$, $U = 75 \text{ V}$ applied voltage are shown in Figure 3d and e. The latter case is just above the threshold of the interfacial instability, and the emergence of the branched fingers is observable. Supplementary Video 3 also illustrates the effect. The protruded parts of the ferroelectric liquid are located on the brighter stripes corresponding to electrode areas as shown in comparison with Figure 3c. Note, that here both the electrode width and gap distances are $10 \mu\text{m}$. Figure 3f illustrates the side view of the electrodes where the gap distance ($180 \mu\text{m}$) is much larger than the electrode width ($10 \mu\text{m}$). Figure 3g shows the corresponding polarizing optical microscopy (POM) image of a sessile droplet above the threshold of the instability with a full-wave plate inserted at 45° with respect to the crossed polarizers. The image clearly shows that the fingers

are located on top of the electrodes, where the fringing field is mostly perpendicular to the substrate (see also Supplementary Video 4).

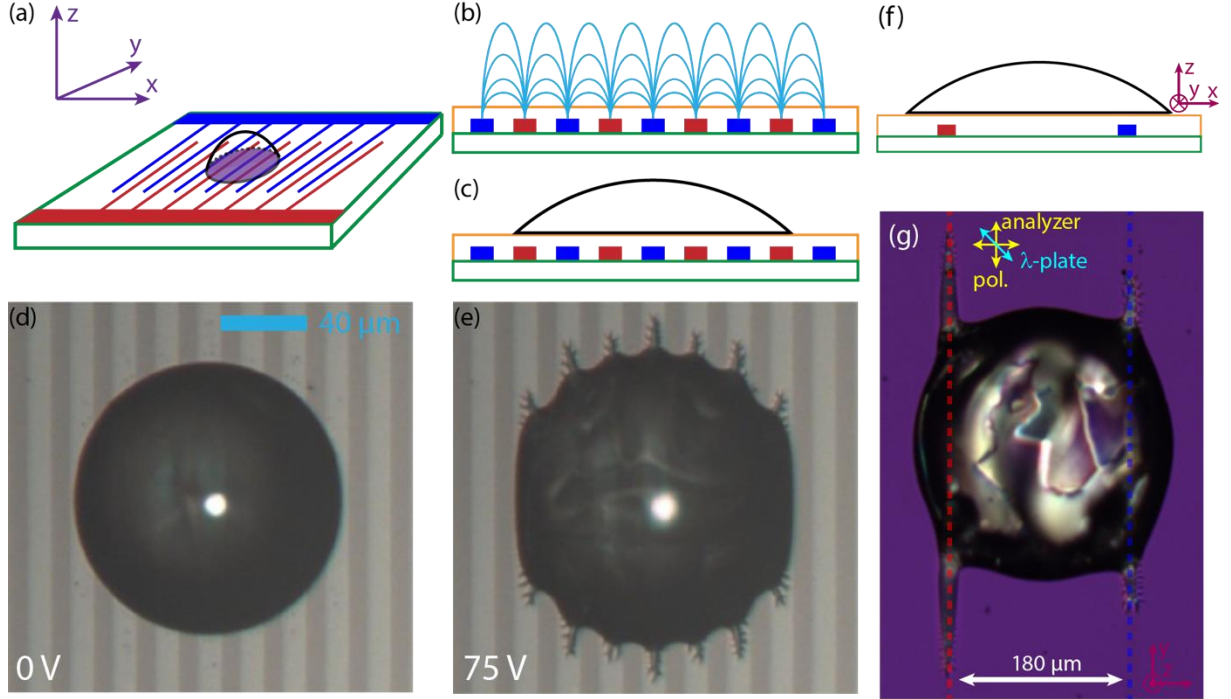


Figure 3: Schematics of the in-plane (G3) electrode geometry and micrographs of the ferroelectric nematic droplet on interdigitated electrodes. (a): Illustration of the interdigitated electrodes with the coordinate system. Side view ($x - z$ plane) of the electrodes with fringing field (b) and the sessile droplet (c). Reflection microscopy image ($x - y$ plane) of the droplet at 0 V (d) and 75 V (e) applied voltage at $f = 10$ kHz. Brighter stripes correspond to the electrode areas. (f) Side view of the geometry with a single thin pair of electrodes with a larger gap between them. (g) The corresponding polarizing microscope image, showing that the fluid fingers spread above the electrodes, where the fringing field is perpendicular to the substrate.

Figure 4 shows the temperature and frequency dependences of the threshold voltages for geometries G2 and G3. Figure 4a shows the temperature dependence of the threshold voltage U_{th} at $f = 1$ kHz, revealing that the emergence of the contact line instability decreases sharply on cooling from the N to the N_F phase. Note, that the transition temperature T_{NN_F} corresponds to the state without voltage. It is known²⁷ that the electric field might shift the transition by several degrees. In the ferroelectric nematic phase, the threshold voltage slightly decreases towards lower temperatures. The small, but clearly distinguishable hysteresis in the voltage dependence of the contact line instability is present in the entire temperature range. The inset of Figure 4a shows Ro_{cl} as function of the applied voltage at $f = 1$ kHz and $T = 127$ °C in the ferroelectric nematic phase. Up to 42 V the roughness is constant in spite of the slight increase of the circumference of the contact line; above 42 V a sharp increase of the roughness clearly indicates the appearance of the spiky structure, and the threshold-like behavior. Decreasing the voltage, a similar behavior is observed with a threshold at 38 V. This weak hysteresis indicates a weakly first order nature of the instability. Quasi-statically

increasing the voltage led to the same pattern as when the voltage was suddenly switched above the threshold from zero.

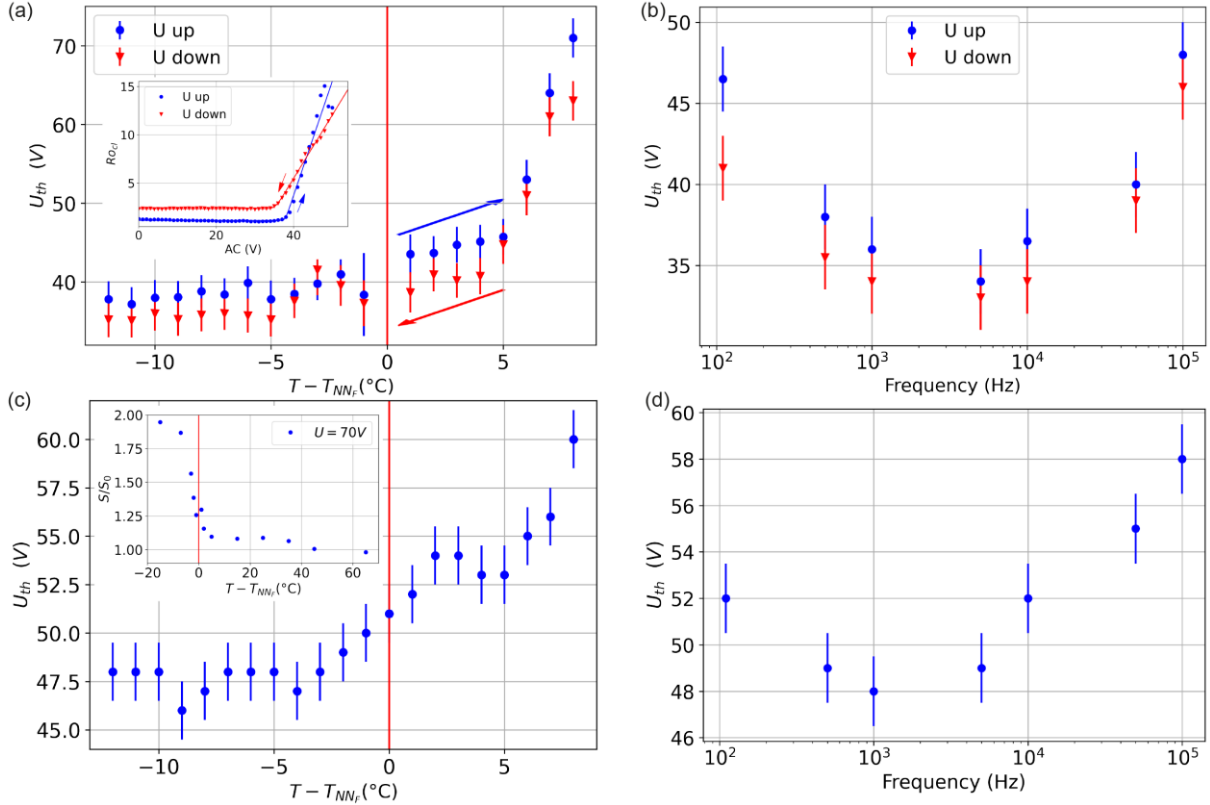


Figure 4 (a) Temperature dependence of the threshold voltage measured at $f = 1$ kHz in the fluid bridge geometry (G2). (a-inset) The roughness of the contact line (Ro_{cl}) of the fluid bridge at one substrate as function of applied voltage at $T = 127$ °C and $f = 1$ kHz. (b) Threshold voltage U_{th} of the interfacial instability as function of frequency at $T = 127$ °C. The threshold voltage of the interfacial instability measured on substrates with interdigitated surface electrodes (G3 geometry) (c) as a function of temperature at $f = 1$ kHz and (d) as a function of frequency at $T = 127$ °C. (c-inset) The normalized circumference S/S_0 of a $125 \mu\text{m}$ diameter droplet as a function of temperature with a constant applied voltage ($U = 75$ V, $f = 10$ kHz).

In Figure 4b, we have plotted the frequency dependence of the threshold voltage in the ferroelectric nematic phase at $T = 127$ °C. In the $f = 100$ Hz – 100 kHz range the lowest thresholds were found at around 10 kHz and U_{th} sharply increases toward the low and high ends of the studied frequency range. The hysteresis between decreasing and increasing voltages was found to be larger at the lower and higher limits in the studied f -range.

The temperature dependence at $f = 1$ kHz and the frequency dependence at $T = 127$ °C of the threshold voltage of the interfacial instability are shown in Figure 4c and Figure 4d, respectively. The temperature dependence at 1 kHz shows a gradual decrease of the threshold voltage while cooling from the N to the N_F phase. Cooling in a constant voltage, the normalized circumference remains near one in the isotropic and the upper part of the nematic range, but it increases sharply already in the N phase before entering to the N_F phase. The inset to Figure 4c shows the temperature dependence of the normalized circumference S/S_0 of a $125 \mu\text{m}$ diameter

droplet for $U = 75$ V, $f = 10$ kHz, where S_0 is the circumference of the drop at the base substrate without applied voltage. One can see that the threshold voltage in the N_F phase has a minimum at around 1 kHz.

Figure 5 shows the electrically induced pattern on wide in-plane electrode pairs, where the electrode width was much higher than the initial droplet diameter and the separation of electrodes. The gap between the electrodes was $180\text{ }\mu\text{m}$ and the diameter of the drop was always larger than the gap. As we increase the applied voltage in this geometry, the drop starts to spread onto the surface of the electrodes, where the electric field has a dominant z -component. During the spreading, several fingers start to grow from the drop evolving to a fractal-like structure as seen in Figure 5c (see also Supplementary Video 5). This effect increases up to 90 V, then at higher voltages the drop starts to spread parallel with electrodes, too (Figure 5d). By applying even higher voltages, the drop continuously spreads along the electrodes and becomes increasingly elongated (see also Supplementary Video 6). It is important to emphasize that the branched structure does not change in time as long as the applied voltage is kept constant. When a series of droplets are deposited in a line between the electrodes, we find that in case of the developed instability the drops are not merged but they repel each other as seen in Figure 5e. A closer look at the POM image taken with a λ -plate sheds light on the molecular arrangement in the branches. In Figure 5f, we can see blue and orange tips meaning parallel and perpendicular orientation of the director with respect to the axis of the λ -plate, respectively. This observation indicates that during the finger growth, the director and thus the spontaneous polarization are aligned along the branches. This explains the electrostatic nature of the repulsion between neighboring fingers facing each other.

Using an image of a well-developed branched structure in the geometry of wide in-plane electrodes, we have determined the Hausdorff or fractal dimension as $d_f \approx 1.95 \pm 0.03$, which strongly indicates the fractal-like property of the structure since $d_f < 2$.²⁸

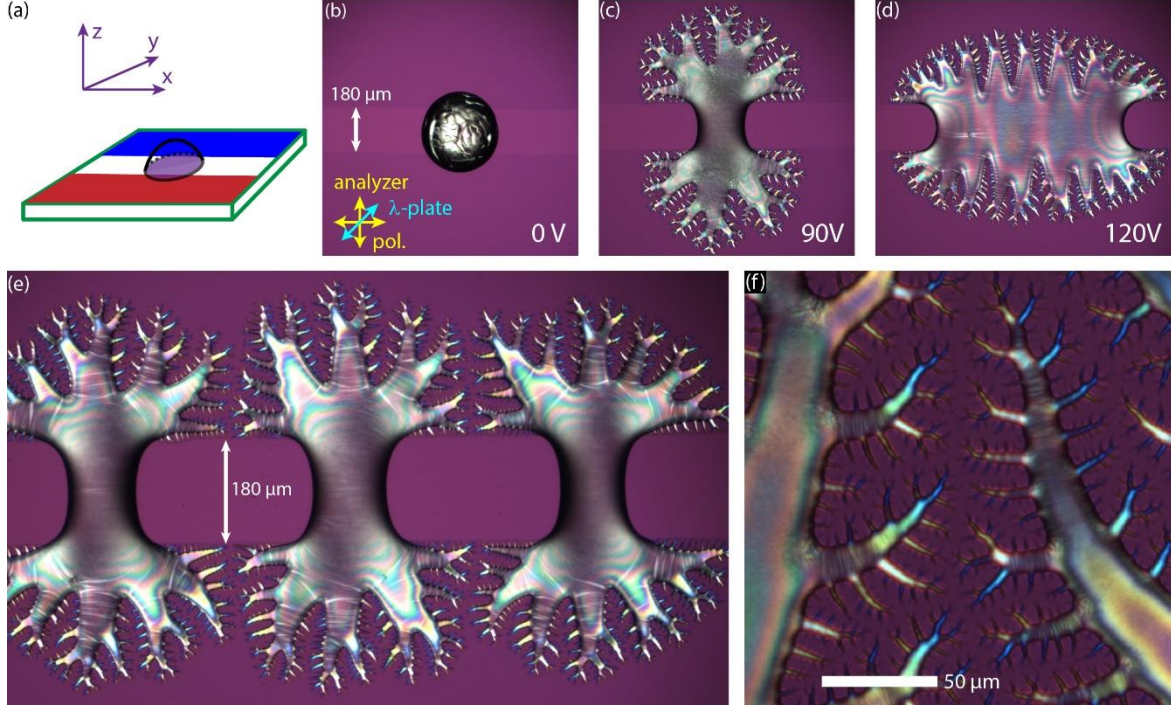


Figure 5: Geometry of the wide in plane electrodes (a). Polarizing optical microscopy images of ferroelectric nematic droplets on surface electrode pairs at 0 V (b), at 90 V (c) and at 120 V (d) with $f = 500$ Hz sinusoidal driving. (e) A series of neighboring droplets showing the instability and interaction. (f) A magnified area near two branches showing that their tips are arranged to maximize the distance between neighbor tips.

To analyze the director structure more quantitatively, we carried out polarimetric microscopy measurements of the tips giving pixelwise information of the average director orientation in the sample plane. In Figure 6a, a typical example is presented, where the map of green rods represents the projection of the director field on the sample plane. The map clearly shows that the director is aligned along the spreading direction of the fingers, which leads to bound charges at the surface that repel each other. We also detected the surface topography of the branched structure in crystallized samples quenched from the ferroelectric nematic phase. A typical result from a white light interferometric profilometer is shown in Figure 6b, where the color-coded height profile is measured from the flat base substrate. We selected one finger from the lowest level of the hierarchical branched structure (see gray dashed line in Figure 6b), and plotted the height profile of it in a cross-sectional view as seen in Figure 6c. We find that the width and height of the finger are about $2 \mu\text{m}$ and $0.5 \mu\text{m}$, respectively. Such dimensions are close to the resolution of our optical microscopy techniques; therefore, we applied scanning electron microscopy (SEM) to reveal the fine structure and tip dimensions the electric field induced fingers using quenched samples. A representative SEM image is shown in Figure 6d, where the branched structure can be observed with finer details. The magnified view of a selected tip presents the submicron radius of curvature ($\sim 0.5 \mu\text{m}$) at the end of the finger.

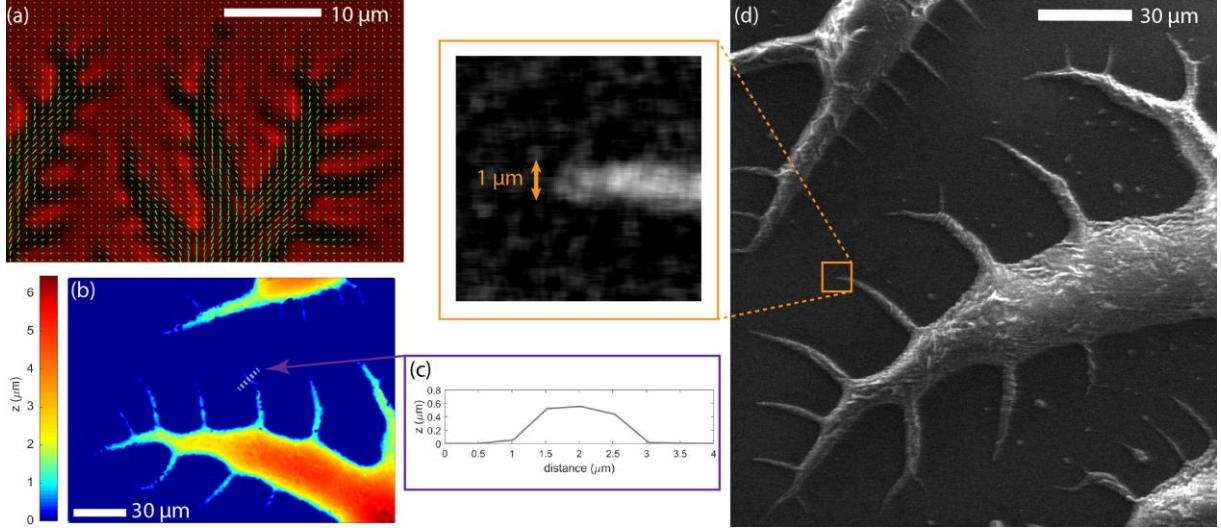


Figure 6: Properties of the tips of the side branches of the ferroelectric nematic liquid crystal sessile droplet above the electrically induced fingering instability. (a) Polarimetric microscopy image of the branched ferroelectric fluid interface on wide surface electrode pairs. Green rods indicate the effective orientation of the director. (b) Surface topography of the branched structure measured by interferometric profilometry. (c) Cross-section of one branch indicated by a dotted gray line. (d) Scanning electron microscopy image of the quenched ferroelectric nematic fluid exhibiting the electric field-induced interfacial instability.

III. Discussion

Our results presented above reveal an AC electric field-induced fingering instability resembling to the Rosensweig²² or normal field instability, which is a well-known interfacial pattern formation phenomenon observed in ferromagnetic fluids, where the horizontal ferrofluid surface becomes unstable above a critical magnitude of vertical magnetic field producing spectacular spiky extrusions^{22,29–31}. Depending on the geometry, such instability can manifest itself in various morphologies, but the basic mechanism was understood as a balance between gravitational, capillary, and magnetic forces. While Rosensweig instability produces spikes normal the free surface, in our case they appear on the bounding plates normal to the electric field. We think the main reason for the difference is that for our small sample sizes the effect of gravity is negligible compared to the surface tension.

On the other hand, a fingering or labyrinthine instability driven by a magnetic field perpendicular to the plates of thin films or the base plates of small droplets where the effect of gravity can be neglected^{32–35}, is more analogous to our experiments³⁶. Such labyrinthine instability was also observed in dielectric fluids exposed to several kilovolts^{29,32,37}. In both types of fields, a required condition for the emergence of the labyrinthine instability is a gap between the ferromagnetic or dielectric fluid and the poles of the magnet or the electrode surface, respectively. By the presence of such gap, a sufficiently large field component in the plane of the bounding substrates at the contact line of the two fluids can arise to induce the instability.

Adopting the theory derived for dielectric fluids³⁷, we calculated the threshold U_c voltage of the labyrinthine instability for our case as

$$U_c = \sqrt{\frac{\pi}{2} \frac{\gamma_w(2L_i+L)(2\varepsilon_m L_i+\varepsilon_i L_i)^2(2\varepsilon_d L_i+\varepsilon_i L_i)^2}{\varepsilon_0(\varepsilon_d-\varepsilon_m)^2 \varepsilon_i^2 L_i L(L_i+L)((\varepsilon_m+\varepsilon_d)L_i+\varepsilon_i L)}}, \quad (1)$$

where ε_d , ε_m , and ε_i are the relative permittivities of the droplet, the surrounding medium, and the insulating SU8 layer, respectively. Considering that the surface tension of SU8 is $\gamma_w = 0.03 \text{ N/m}$ ³⁸, $\varepsilon_d = 10000$ ⁴, $\varepsilon_m = 1$, $\varepsilon_i = 4$ ³⁹, $L = 74 \text{ }\mu\text{m}$, and $L_i = 1.4 \text{ }\mu\text{m}$, we get $U_c \approx 13 \text{ V}$. This value is smaller than $\sim 40 \text{ V}$ that we got for the threshold in geometry G2. The difference could be attributed to several factors, such as the finite ($\sigma \sim 10^{-6} \text{ S/m}$) electric conductivity of the N_F material that Eq.(1) neglects, the issues with the interpretation of the dielectric constant⁴⁰ and not taking into account the depolarizing internal electric field $\vec{E}_i = -\frac{\vec{P}}{\varepsilon_0 \varepsilon}$ arising due to the ferroelectric polarization.

The results in geometry G1, when external electric field was applied normal to the base plate of sessile droplets, are very similar to that observed^{23,25,26} when the sessile droplets were placed on a lithium niobate ferroelectric crystal surface, indicating a Rayleigh-type instability in which droplets exhibit the sudden emission of fluid jets with electric charging beyond a threshold. In those ferroelectric sessile droplets, the bulk LC polarization P_s spontaneously self-organizes in response to the external electric field provided by the fringing electric field of the ferroelectric crystal.

Our experiments differ in several respects. (i) Our droplets and bridges do not sense the DC fringing field of a ferroelectric crystal, but we apply external AC fields either normal to the base plate or in-plane. (ii) In the in-plane geometries (G2 – see Figure 3 and Figure 5) the fingers are moving into the electrode area where the field is perpendicular to the substrate. Accordingly, for all geometries the instability along the base substrate is due to a field that is perpendicular to the substrates just as in²³.

In the G1 geometry (Figure 1a), assuming the LC droplet is perfect insulator, the internal electric field E_i is scaled down by the ratio of the dielectric constant of the droplet ε_d and the surrounding medium ε_m as $\vec{E}_i = \frac{\vec{E}_o}{1+N(\varepsilon_d/\varepsilon_m-1)}$, where N is the depolarization factor. For spheroid with the rotational axis c being along the field, N depends on the ratio c/a , where a is the radius at the base plate. Specifically, when $c \ll a$, then $N \approx 1$ and $\vec{E}_i \approx \frac{\vec{E}_o \cdot \varepsilon_m}{\varepsilon_b}$ ⁴¹. It has been shown recently that for a hemispheroid the internal electric field is very close to that of a spheroid⁴². Approximating our spherical cap with a shallow hemispheroid, we obtain that the

internal field in the LC sessile droplet is roughly inversely proportional to the effective dielectric constant, which is close to ε_{\perp} , i.e., $E_i \approx \frac{E_o}{\varepsilon_{\perp}} = \frac{U}{L\varepsilon_{\perp}}$.

Assuming that the induced polarization ΔP will compensate the internal field $E_i = -\frac{\Delta P}{\varepsilon_o \varepsilon_{\perp}}$, we get that $\Delta P \approx \frac{U \cdot \varepsilon_o}{L} \sim 10^{-5} \text{ C/m}^2$, i.e., the same order of magnitude as estimated by Barboza et al.²³ for droplets on ferroelectric crystal plates.

Following the arguments in ²³, we assume that the instability starts in a topological defect with surface area S and charge accumulation of $q = 2P_s S$. The condition for the finger formation is that the repulsive force $F_C = \frac{kqQ}{l^2}$, where l is acting on the tip with radius r and length l should overcome the force arising from the surface tension, $F_S \sim \gamma \pi r$. With $k \approx 9 \cdot 10^9 \frac{\text{Nm}^2}{\text{C}^2}$, $q = P\pi r^2/2$ and $Q = \Delta P \cdot R^2 \pi$, where R is the radius of the base plane of the droplet and $\Delta P \approx \frac{U \cdot \varepsilon_o}{L} = E_o \varepsilon_o$ we get the condition for the external electric field E_o that $E_o > \frac{2\gamma l^2}{\pi k P r \varepsilon_o R^2} \geq \frac{2\gamma}{\pi k P r \varepsilon_o}$. At 5 °C below the $N - N_F$ transition $P_o \sim 4 \cdot 10^{-2} \text{ C/m}^2$ ³, and assuming $\gamma \sim 0.03 \text{ N/m}$, we get that $E_o \sim \frac{6}{r} \cdot \frac{l^2}{R^2}$. Figure 1c shows that at 220 V the length of the tips with radii of $r \sim 1 \mu\text{m}$. This gives $U_{th} \sim \frac{6L}{r} \text{ V} = 6 \cdot \frac{150}{1} \text{ V} \sim 900 \text{ V}$, which is in the order of magnitude what we found in the experiments.

In summary, we presented pattern forming instabilities of sessile droplets and fluid bridges of a ferroelectric nematic liquid crystal in externally applied electric fields. The fingering instability observed above is similar to Rayleigh-type instability observed in charged droplets in electric fields or labyrinth-type instabilities observed in ferromagnetic liquids in magnetic fields. The nematic director and ferroelectric polarization direction was found to point along the tip of the fingers that appear to repel each other, indicating that the ferroelectric polarization is essentially parallel to the director.

IV. Methods

In our studies, we used (4-[(4-nitrophenoxy)carbonyl] phenyl-2,4-dimethoxybenzoate (RM734), one of the prototype compounds for ferroelectric nematic materials^{4,8,9}). The sessile liquid crystal droplets were prepared in the nematic phase (at $\sim 170^\circ \text{C}$) by a custom-made setup allowing simultaneous microscopic observations in both horizontal and vertical directions by applying two Questar QM100 long-range microscopes with a Canon EOS450D and a Hayear HY-500B camera. Positioning of droplets was done in a heated environment (with temperature

stability better than 0.1 °C) by a micromanipulator arm. The experiments on the droplets were carried out by using a Leica DMRX polarizing microscope equipped with a Linkam LTS350 hot stage and a TMS94 controller providing a temperature stability of 0.01°C.

In all our sample geometries we have used either plain or patterned indium-tin-oxide (ITO) coated glass plates as electrodes, which were coated by a 1.4 µm thick layer of SU8-3000 (Kayaku Microchem) hard baked photoresist to prevent direct charge transfer. We note that there is a significant effect of the thickness of the SU8 layer on the electrodes due to its effect on the voltage distribution along z . In case of the liquid bridge geometry, the threshold voltage for the Freedericksz transition in the nematic phase of RM734 was 40 V with 1.4 µm thick SU8 coatings on the electrodes, while for 260 nm thick insulator layer, this threshold was found to be as low as 1 V. The contact angle of RM734 on SU8 was found to be $\theta_c \approx 41^\circ$.

For scanning electron microscopy and optical profilometry measurements, the sample in the N_F phase was quenched by suddenly dropping it into liquid nitrogen while the electric field was applied onto it. Rapid solidification preserved the fine branched structure of the ferroelectric nematic fluid. Scanning electron micrographs were recorded with a TESCAN MIRA3 scanning electron microscope equipped with a field-emission gun. Since the solidified LC samples are electrically insulating, the low-vacuum mode was applied with 40 Pa nitrogen pressure to suppress the charging of the sample. Under these circumstances, images with sufficient resolution could be obtained in the 5-8 kV acceleration voltage range. An LVTSD detector was used to obtain secondary electron images. Optical profilometry measurements were performed with a Zygo NewView 7100 3D white light interferometric profiler using Mirau interferometric objectives. Polarimetric microscopy measurements were performed by applying a Thorlabs Kiralux CS505MUP polarization camera in a custom-made microscope with circularly polarized monochromatic illumination (at 660 nm wavelength) in transmission mode.

To precisely analyse the voltage dependence of this instability, we applied a geometrical transformation, mapping a band around the contact line to a line (Fig2 (c)). To transform the surface of the drop to a straight line, first the undeformed drop was fitted by an ellipsoid, then the images close to the surface of the drop were plotted. We define the roughness of the contact lines for a given voltage as $Ro_{cl} = \sum_{\varphi} |\partial_{\varphi}^2 \sum_r I(r, \varphi)|$, where $I(r, \varphi)$ is the pixel intensity map of the image as a function of the radius r and the azimuthal angle φ . ∂_{φ}^2 denotes the second derivate and the sum was calculated in the surroundings of the contact line. The voltage

dependence of the roughness of the contact lines was fitted by the function⁴³ $f(U) = a \cdot \ln(1 + e^{b/e \cdot (U - U_{\text{th}})}) + d$, where U_{th} is the threshold voltage, a , b , and d are fit parameters.

The fractal dimension was determined by image analysis applying the box counting algorithm implemented in Python.

Acknowledgement

This work was financially supported by the Hungarian National Research, Development, and Innovation Office under grant NKFIH FK142643 and the US National Science Foundation under grant DMR-2210083. This paper was supported by the János Bolyai Research Scholarship of the Hungarian Academy of Sciences. We are thankful to Ewa Körblova and David Walba at University of Colorado at Boulder for providing RM734 for us. We thank Attila Nagy and Aladár Czitrovsky for providing access to the optical profilometer.

References

1. de Gennes, P. G. & Prost, J. *The Physics of Liquid Crystals*. (Oxford University Press, 1993).
2. Yang, D.-K. & Wu, S.-T. *Fundamentals of Liquid Crystal Devices*. (John Wiley & Sons Ltd, 2006).
3. Chen, X. *et al.* First-principles experimental demonstration of ferroelectricity in a thermotropic nematic liquid crystal: Polar domains and striking electro-optics. *Proc Natl Acad Sci U S A* **117**, 14021–14031 (2020).
4. Sebastián, N., Čopič, M. & Mertelj, A. Ferroelectric nematic liquid-crystalline phases. *Phys Rev E* **106**, 21001 (2022).
5. Born, M. Über anisotrope Flüssigkeiten: Versuch einer Theorie der flüssigen Kristalle und des elektrischen Kerr-Effekts in Flüssigkeiten. *Sitzungsber. Preuss. Akad Wiss* **30**, 614–650 (1916).
6. Lavrentovich, O. D. Ferroelectric nematic liquid crystal, a century in waiting. *Proc Natl Acad Sci U S A* **117**, 14629–14631 (2020).
7. Nishikawa, H. *et al.* A Fluid Liquid-Crystal Material with Highly Polar Order. *Advanced Materials* **29**, 1702354 (2017).

8. Mandle, R. J., Cowling, S. J. & Goodby, J. W. A nematic to nematic transformation exhibited by a rod-like liquid crystal. *Physical Chemistry Chemical Physics* **19**, 11429–11435 (2017).
9. Mandle, R. J., Cowling, S. J. & Goodby, J. W. Rational Design of Rod-Like Liquid Crystals Exhibiting Two Nematic Phases. *Chemistry - A European Journal* **23**, 14554–14562 (2017).
10. Mertelj, A. *et al.* Splay Nematic Phase. *Phys Rev X* **8**, 041025 (2018).
11. Sebastián, N. *et al.* Ferroelectric-Ferroelastic Phase Transition in a Nematic Liquid Crystal. *Phys Rev Lett* **124**, 037801 (2020).
12. Pleiner, H. & Brand, H. R. Spontaneous splay phases in polar nematic liquid crystals. *Europhys. Lett.* **9**, 243–249 (1989).
13. Manabe, A., Bremer, M. & Kraska, M. Ferroelectric nematic phase at and below room temperature. *Liq Cryst* **48**, 1079–1086 (2021).
14. Zhao, X. *et al.* Spontaneous helielectric nematic liquid crystals: Electric analog to helimagnets. *Proceedings of the National Academy of Sciences* **118**, e2111101118 (2021).
15. Saha, R. *et al.* Multiple ferroelectric nematic phases of a highly polar liquid crystal compound. *Liq Cryst* 1–13 (2022) doi:10.1080/02678292.2022.2069297.
16. Yadav, N., Panarin, Y. P., Vij, J. K., Jiang, W. & Mehl, G. H. Polar nature of the ferroelectric nematic studied by dielectric spectroscopy. *ArXiv* 2203.04944 (2022) doi:10.48550/arxiv.2203.04944.
17. Nishikawa, H. *et al.* Nano-Clustering Mediates Phase Transitions in a Diastereomerically-Stabilized Ferroelectric Nematic System. *ArXiv* 2205.04848 (2022).
18. Brown, S. *et al.* Multiple Polar and Non-polar Nematic Phases. *ChemPhysChem* **22**, 2506–2510 (2021).
19. McHale, G., Brown, C. v., Newton, M. I., Wells, G. G. & Sampara, N. Dielectrowetting driven spreading of droplets. *Phys Rev Lett* **107**, 186101 (2011).
20. McHale, G., Brown, C. v. & Sampara, N. Voltage-induced spreading and superspreading of liquids. *Nat Commun* **4**, 1605–1607 (2013).
21. Edwards, A. M. J., Brown, C. v., Newton, M. I. & McHale, G. Dielectrowetting: The past, present and future. *Curr Opin Colloid Interface Sci* **36**, 28–36 (2018).
22. Cowley, M. D. & Rosensweig, R. E. The interfacial stability of a ferromagnetic fluid. *J Fluid Mech* **30**, 671–688 (1967).

23. Barboza, R. *et al.* Explosive electrostatic instability of ferroelectric liquid droplets on ferroelectric solid surfaces. *Proceedings of the National Academy of Sciences* **119**, e2207858119 (2022).
24. Rayleigh, Lord. XX. On the equilibrium of liquid conducting masses charged with electricity. *The London, Edinburgh, and Dublin Philosophical Magazine and Journal of Science* **14**, 184–186 (1882).
25. Cmok, L. *et al.* Running streams of a ferroelectric nematic liquid crystal on a lithium niobate surface. *ArXiv* 2209.05140 (2022) doi:10.48550/arxiv.2209.05140.
26. Cmok, L. *et al.* Light-induced dynamics of liquid-crystalline droplets on the surface of iron-doped lithium niobate crystals. *ArXiv* 2208.02318 (2022) doi:10.48550/arxiv.2208.02318.
27. Gorecka, E. Intrinsically chiral ferronematic liquid crystals. *28th International Liquid Crystal Conference (ILCC), Lisbon Preprint at* (2022).
28. Barabási, A.-L. & Stanley, H. E. *Fractal Concepts in Surface Growth*. (Cambridge University Press, 1995). doi:10.1017/CBO9780511599798.
29. Ronald E. Rosensweig. *Ferrohydrodynamics*. (Cambridge University Press, 1985).
30. Blums, E., Cebers, A. & Maiorov, M. M. *Magnetic Fluids*. (De Gruyter, 1997). doi:10.1515/9783110807356.
31. Bacri, J.-C. & Salin, D. First-order transition in the instability of a magnetic fluid interface. *J. Physique Lett.* **45**, 559–564 (1984).
32. Rosensweig, R. E., Zahn, M. & Shumovich, R. Labyrinthine instability in magnetic and dielectric fluids. *J Magn Magn Mater* **39**, 127–132 (1983).
33. Hillier, N. J. & Jackson, D. P. Width of a ferrofluid finger: Hysteresis and a double energy minimum. *Phys Rev E Stat Nonlin Soft Matter Phys* **75**, 036314 (2007).
34. Igonin, M. & Cebers, A. Labyrinthine instability of miscible magnetic fluids. *Physics of Fluids* **15**, 1734 (2003).
35. Richardi, J., Ingert, D. & Pileni, M. P. Labyrinthine instability in magnetic fluids revisited. *Journal of Physical Chemistry B* **106**, 1521–1523 (2002).
36. Jackson, D. P., Goldstein, R. E. & Cebers, A. O. Hydrodynamics of fingering instabilities in dipolar fluids. *Phys Rev E* **50**, 298 (1994).
37. Zahn, M. & Shumovich, R. Labyrinthine Instability in Dielectric Fluids. *IEEE Trans Ind Appl* **IA-21**, 53–61 (1985).

38. Saravanan, P., Satyanarayana, N. & Sinha, S. K. SU-8 Composite Based “Lube-tape” for a Wide Range of Tribological Applications. *Micromachines* 2014, Vol. 5, Pages 263-274 **5**, 263–274 (2014).
39. Lapeyronie, C., Alfonso, M. S., Viala, B. & Tortai, J.-H. Superior dielectric properties of epoxy-based photoresist thin film nanocomposites with carbon-coated Cu@C nanoparticles. *Mater Res Express* **9**, 106301 (2022).
40. Clark, N. A., Chen, X., MacLennan, J. E. & Glaser, M. A. Dielectric spectroscopy of ferroelectric nematic liquid crystals: Measuring the capacitance of insulating interfacial layers. *ArXiv* 2208.09784 (2022) doi:10.48550/arxiv.2208.09784.
41. Karaszi, Z., Salamon, P., Buka, Á. & Jákli, A. Lens shape liquid crystals in electric fields. *J Mol Liq* **334**, 116085 (2021).
42. Stubbe, M. & Gimsa, J. Furthering the state of knowledge on the electric properties of hemi-ellipsoidal single cells and cell patches on electrodes. *Biosens Bioelectron* **105**, 166–172 (2018).
43. Liu, Y.-W. & Neely, S. T. Suppression tuning of distortion product otoacoustic emissions in humans: results from cochlear mechanics simulation. *J Acoust Soc Am* **131**, 3306 (2012).